Computer Physics Communications 196 (2015) 599–610

Contents lists available at ScienceDirect

Computer Physics Communications

journal homepage: www.elsevier.com/locate/cpc

Calibration of optical tweezers with non-spherical probes via high-resolution detection of Brownian motion☆

A. Butykai [a,*], F.M. Mor [b], R. Gaál [b], P. Domínguez-García [c], L. Forró [b], S. Jeney [b]

[a] Department of Physics, Budapest University of Technology and Economics and MTA-BME Lendület Magneto-optical Spectroscopy Research Group, 1111 Budapest, Hungary

[b] Laboratory of Physics of Complex Matter, École Polytechnique Fédérale de Lausanne, CH-1015 Lausanne, Switzerland

[c] Dep. de Física de Materiales, Universidad Nacional de Educación a Distancia (UNED), Madrid 28040, Spain

ARTICLE INFO

Article history:
Received 9 April 2015
Received in revised form
25 June 2015
Accepted 30 June 2015
Available online 26 July 2015

Keywords:
Calibration of optical tweezers
Non-spherical probe
Brownian motion
Power spectral density (PSD)
Mean square displacement (MSD)
Velocity autocorrelation function (VAF)

ABSTRACT

Optical tweezers are commonly used and powerful tools to perform force measurements on the piconewton scale and to detect nanometer-scaled displacements. However, the precision of these instruments relies to a great extent on the accuracy of the calibration method. A well-known calibration procedure is to record the stochastic motion of the trapped particle and compare its statistical behavior with the theory of the Brownian motion in a harmonic potential. Here we present an interactive calibration software which allows for the simultaneous fitting of three different statistical observables (power spectral density, mean square displacement and velocity autocorrelation function) calculated from the trajectory of the probe to enhance fitting accuracy. The fitted theory involves the hydrodynamic interactions experimentally observable at high sampling rates. Furthermore, a qualitative extension is included in our model to handle the thermal fluctuations in the orientation of optically trapped asymmetric objects. The presented calibration methodology requires no prior knowledge of the bead size and can be applied to non-spherical probes as well. The software was validated on synthetic and experimental data.

Program summary

Program title: PFMCal

Catalogue identifier: AEXH_v1_0

Program summary URL: http://cpc.cs.qub.ac.uk/summaries/AEXH_v1_0.html

Program obtainable from: CPC Program Library, Queen's University, Belfast, N. Ireland

Licensing provisions: Standard CPC licence, http://cpc.cs.qub.ac.uk/licence/licence.html

No. of lines in distributed program, including test data, etc.: 206,399

No. of bytes in distributed program, including test data, etc.: 10,319,465

Distribution format: tar.gz

Programming language: MatLab 2011a (MathWorks Inc.).

Computer: General computer running MatLab (MathWorks Inc.), using Statistics Toolbox.

Operating system: Any which supports Matlab using Statistics Toolbox.

RAM: 10 MB

Classification: 3, 4.9, 18, 23.

Nature of problem: Calibration of optical tweezers by measuring the Brownian motion of the trapped object. The voltage-to-displacement ratio of the detection system (the inverse of the sensitivity), the

☆ This paper and its associated computer program are available via the Computer Physics Communication homepage on ScienceDirect (http://www.sciencedirect.com/science/journal/00104655).

* Corresponding author.
E-mail address: butykai@dept.phy.bme.hu (A. Butykai).

http://dx.doi.org/10.1016/j.cpc.2015.06.024

stiffness of the trap and the size of the bead are obtained via the simultaneous fitting of the power spectral density (PSD), mean square displacement (MSD) and velocity autocorrelation (VAF) functions calculated from the trajectory. The calibration can be performed for non-spherical probes as well.

Solution method: Initialization points for all parameters are inferred from characteristic features of the statistical observables (PSD, MSD and VAF) based on the method developed by Grimm et al. in [1]. Theoretical functions for the PSD, the MSD and the VAF are calculated from the model of Brownian motion confined by a harmonic potential taking hydrodynamic interactions into consideration [2–4]. This calibration methodology has been successfully used in actual experiments with micro-spheres [5, 6]. Calculated functions are fitted to the measurement data via the Levenberg–Marquardt least square fitting routine available in the MatLab Optimalization Toolbox, using the **nlinfit** function. If the error to the measured data has been estimated, the corresponding data values can be weighted by the inverse of the standard error squared in order to eliminate bias introduced by heteroscedasticity. In order to increase robustness and avoid convergence to local minima, minimum search from multiple initial values in the vicinity of the first guess is possible.

Additional comments: Input of the program is the experimental PSD^{exp}, MSD^{exp}, and VAF^{exp} data points calculated from the measured x, y and z projections of the trajectory of the particle. The data may best be blocked and may optionally contain an error for each data point for better results. The data should be formatted into three columns: 1. independent variables (time or frequency array), 2. function values, 3. optionally, error values (e.g. standard error calculated from the binning) to improve fitting efficiency. In case error values were not estimated, the third column should be filled with zeros. The first row is reserved for a header, data is read from the second row. Data size should not be larger than a few hundreds of rows, otherwise, using larger blocks for binning is advised. In order to observe the short time behavior of the Brownian motion, influenced by hydrodynamic effects, the sampling rate should be typically higher than 100 kHz. Total sampling time is typically tens of seconds, to achieve a good resolution in the frequency range. The optical axis of the laser, the microscope and the detector system should be co-aligned to exclude artificial crosstalk between the x, y and z channels of the position detector.

Running time: Seconds

References:

[1] M. Grimm, T. Franosch, and S. Jeney. High-resolution detection of Brownian motion for quantitative optical tweezers experiments. Phys. Rev. E, 86:021912, Aug 2012.
[2] R. Zwanzig and M. Bixon. Hydrodynamic theory of the velocity correlation function. Physical Review A, 2(5):2005, 1970.
[3] E.J. Hinch. Application of the Langevin equation to fluid suspensions. Journal of Fluid Mechanics, 72:499–511, 12 1975.
[4] H. Clercx and P Schram. Brownian particles in shear. flow and harmonic potentials: A study of long-time tails. Physical Review A, 46(4):1942, 1992.
[5] P. Domínguez-García, F. Cardinaux, E. Bertseva, L. Forró, F. Scheffold, and S. Jeney, Accounting for inertia effects to access the high-frequency microrheology of viscoelastic fluids, Phys. Rev. E, vol. 90, p. 060301, Dec 2014.
[6] P. Domínguez-García, F.M. Mor, L. Forró, and S. Jeney, Exploiting the color of Brownian motion for high-frequency microrheology of Newtonian fluids, Proc. SPIE 8810 (2013) 881015–881015-6.

1. Introduction

Calibration of optical tweezers is essential for quantitative force and displacement measurements. In general, optical tweezers consist of a highly focused laser beam, generating a large electric field gradient, which attracts a dielectric probe towards the focal point [1]. Several different schemes exist to track the position of the trapped object, including video-based detection [2], polarization interferometry [3] or back focal plane interferometry [4–6]. The task of the calibration is to convert the detected signals, most frequently measured as a voltage, to displacement units and to define the force exerted by the optical trap on the probe displaced from its equilibrium position. Within the small vicinity of the equilibrium, the potential energy of the particle is a quadratic function of the displacement, resulting in a harmonic restoring force. Therefore the force can be quantified by assigning a spring constant to the trap and measuring the displacement of the particle. Since the trapping potential is generally anisotropic, the trap must be calibrated in all three dimensions. The spring constants and voltage-to-displacement ratios (inverse sensitivities of the detector system) along the different axes are very often calibrated by recording the Brownian fluctuations of the probe and fitting its statistical behavior. Quantitative optical trapping experiments are typically restricted to spherical probes of known size, because calibration can then be done straightforwardly through comparison with the well-known theory of the isotropic translational Brownian motion [4,7,8].

Nevertheless, non-spherical objects, for instance single crystals [9,10] and biological systems [11] play a key role in optical trapping experiments. Furthermore, elongated probes, such as nanowires are promising candidates for high spatial resolution imaging and force measurements on the subpiconewton scale [12,13]. Therefore, recently increasing attention has turned towards the calibration for non-spherical objects [9,10,12–15]. Here we present a calibration software that utilizes the full-scale hydrodynamic description of the translational Brownian motion, with a qualitative extension to account for the effects of the rotational fluctuations. To formulate a simplified model, we start

from the most general form of the linear detector response when non-spherical probes are used, and exclude several cross-coupling terms in cases that are most relevant in practical applications. For instance, axially symmetric probes, like cylinders and prolate ellipsoids are adequately handled by this model [13]. Under these circumstances, we consider only one angular component of rotational fluctuations with dominant contribution in the detected signal, and assume that for small displacements it is independent of the translational Brownian motion. We found that even the behavior of highly asymmetric, randomly shaped glass particles could be well fitted by our model.

In order to achieve an augmented accuracy in the calibration, our methodology exploits the characteristic nature of the PSD, the MSD and the VAF at different timescales, fitting all three functions simultaneously. Fitting solely the power spectral density of the Brownian motion might lead to ambiguous results due to the correlation of the fitting parameters. Owing to the very distinct short-time characteristics of the VAF, its inclusion in the calibration proves highly efficient. The software was tested on both synthesized and measured data. The analysis showed good consistency between fitted and known parameters.

2. Experimental data

The calibration is performed by fitting the theoretical PSD, MSD and VAF functions to the experimental data. Users must provide these observables calculated from the measured trajectory of the particle $(S_{i,1}, S_{i,2}, \ldots, S_{i,N})$. Here, i refers to the orthogonal coordinate axes x, y and z, in the frame of the photodetector. The experimental observables are computed as:

$$\mathrm{PSD}_i^{\mathrm{exp}}(f) = 2\frac{\left|\hat{S}_i(f)\right|^2}{Nf_S}, \tag{1}$$

where $\hat{S}_i(f)$ is the discrete fast Fourier transform of the detected trajectory. N is the total number of data points and f_S is the sampling frequency. The MSD and VAF data at a lag-time, t are defined by:

$$\mathrm{MSD}_i^{\mathrm{exp}}(t) = \left\langle (S_{i,\tau+t} - S_{i,\tau})^2 \right\rangle_\tau = \frac{1}{N-t}\sum_{\tau=1}^{N-t}(S_{i,\tau+t} - S_{i,\tau})^2 \tag{2}$$

$$\mathrm{VAF}_i^{\mathrm{exp}}(t) = \left\langle v_{i,\tau+t} v_{i,\tau} \right\rangle_\tau = \frac{1}{\Delta t^2}\frac{1}{N-t-1}\sum_{\tau=1}^{N-t-1}(S_{i,\tau+1} - S_{i,\tau})(S_{i,\tau+1+t} - S_{i,\tau+t}), \tag{3}$$

where the second lower indices t and τ represent the discrete sequential numbers associated to the time of the respective data points, and $\Delta t = 1/f_S$ is the time resolution of the measurement. The calculated raw functions (1)–(3) should be binned to reduce the size of the data. In terms of the central limit theorem, averaging a sufficiently large number of data points in each bin allows for the Gaussian estimation of the distribution of the binned data [7]. The standard error is then given by $\Delta y = s_y(i)/\sqrt{N_b(i)}$, where y refers to the PSD, MSD or VAF data, $N_b(i)$ represents the number of data points and $s_y(i)$ is an unbiased estimation of the standard deviation of the points, σ_y in the ith bin. Care must be taken in case of correlated data such as the MSD and VAF, to avoid underestimation of the actual standard deviation due to the reduced number of independent data points. Correlations can be eliminated by consecutive blocking transformations by finding the fixed point of the estimated standard errors [16].

The software accepts any set of the three observables as input. Providing all of them typically improves the efficiency of the fitting. PSD, MSD and VAF data can be loaded from separate text files. The data should be formatted into three columns in the form of $\left[\mathbf{f}; \mathbf{PSD}^{\mathrm{exp}}; \boldsymbol{\Delta PSD}\right]$, $\left[\mathbf{t}; \mathbf{MSD}^{\mathrm{exp}}; \boldsymbol{\Delta MSD}\right]$ and $\left[\mathbf{t}; \mathbf{VAF}^{\mathrm{exp}}; \boldsymbol{\Delta VAF}\right]$ respectively. The third column represents the estimated errors assigned to the data values. If error data are not available, the third column should be filled with zeros. The first row of the data files are reserved for column headers, therefore numerical data is read from the second row by the software.

3. Theoretical functions

In the back focal plane interferometric detection scheme, utilizing a quadrant photodetector (QPD), S_x, S_y and S_z voltages are respectively measured as the differential intensity of the left and right halves, upper and lower halves and the total intensity of the interference pattern projected to the sensor [6]. Ideally, these signals are proportional to the displacements of the probe in the corresponding directions with no crosstalk between the three channels. However, when a non-spherical particle is captured, its angular displacements will also alter the interference pattern, giving a contribution to the measured signals [12]. Also, an artificial crosstalk can arise between the channels due to the arbitrary shaped interference pattern on the QPD. In general the detector signal in the linear regime reads as:

$$S_i(t) = \sum_{j=1}^{3}\alpha_{ij}X_j(t) + \sum_{j=1}^{3}\alpha_{i\Theta_j}\Theta_j(t), \tag{4}$$

where α_{ij} and $\alpha_{i\Theta_j}$ represent the general elements of the translational and rotational sensitivity matrices, and $X_j(t)$ and $\Theta_j(t)$ are the Brownian translation in j direction and Brownian rotation around j, respectively.

In case of spherical probes, the crosstalk between the detector channels – represented by the off-diagonal α_{ij} components – due to an optical misalignment can be eliminated via a linear transformation of the coordinates of the detected trajectory [7] or alternatively, it can be accounted for in the fitting model as described in [17]. Nevertheless, when physical rotation is involved, the cross-coupling effect of the rotation and the optical misalignment cannot be easily distinguished. Therefore, before non-spherical particles are used, the careful alignment of the optical path with a spherical probe is essential for obtaining unambiguous results [18].

The model can be further simplified if only one rotational component gives a significant contribution to the detector signals. This has been shown for elongated, axially symmetric probes [13], which are promising candidates for uses in ultra-sensitive photonic force microscopy. In this study we examined the Brownian motion of randomly shaped microscopic glass splinters, which was also well-fitted by a single rotational component superimposed to the translational fluctuations. We attribute this additional term to the stochastic rotations around the optical axis. Assuming that the detector response is proportional to the change in the orthogonal projection of the probe to the detector axes, and the angular fluctuations are small ($\Theta(t) \ll 1$), the detected signal simplifies to:

$$S_i(t) = \alpha_{ii}X_i(t) + \alpha_{i\Theta}\Theta(t), \tag{5}$$

where $\Theta(t)$ is the relevant stochastic rotational process. In the small displacement and rotation limit, translational and angular fluctuations may be regarded as independent, thus the observables (1)–(3) decompose to a sum of purely translational and rotational components:

$$\beta_{ii}^2\mathrm{PSD}_i^{\mathrm{exp}}(f) = \mathrm{PSD}_i(f) + \beta_{ii}^2\alpha_{i\Theta}^2\mathrm{PSD}_\Theta(f), \tag{6}$$

$$\beta_{ii}^2\mathrm{MSD}_i^{\mathrm{exp}}(t) = \mathrm{MSD}_i(t) + \beta_{ii}^2\alpha_{i\Theta}^2\mathrm{MSD}_\Theta(t), \tag{7}$$

$$\beta_{ii}^2\mathrm{VAF}_i^{\mathrm{exp}}(t) = \mathrm{VAF}_i(t) + \beta_{ii}^2\alpha_{i\Theta}^2\mathrm{VAF}_\Theta(t), \tag{8}$$

where we introduced $\beta_{ii} = 1/\alpha_{ii}$, the inverse of the translational sensitivity elements, referred to as voltage-to-displacement conversion factors. Using this form provides the calibrated observables in displacement units instead of voltages, as will be displayed throughout this paper. From Eqs. (6)–(8) it concludes that two independent relaxational processes are distinguishable in the observables, one originating from the translational and the second from the rotational fluctuations, restored by the optical forces and torques, respectively. We note that a similar additional relaxational process has been observed for optically trapped probes in Maxwell fluids owing to the elasticity of the medium [19], which can also be handled by the same model.

3.1. Translational Brownian motion

Although the parameters of the optical trap are generally anisotropic, hereafter we consider one direction only, neglecting i indices for the sake of brevity. The translational Brownian motion is most accurately described – beyond the Ornstein–Uhlenbeck theory – when accounting for the inertia of the fluid displaced by the fluctuating particle [20]. As pointed out by Lukic et al. in [21], neglecting the emerging hydrodynamic effects may introduce significant error to the calibration. The stochastic motion of the trapped probe can be divided into three characteristic time regimes, which depend on the physical properties of the particle and the medium [22]. The time scale $\tau_p = 2R_p^2\rho_p/(9\eta_f)$ separates the ballistic motion from the diffusive behavior. Hydrodynamic backflow effects become relevant near $\tau_f = R_p^2\rho_f/\eta_f$. Finally, the restoring force confining the free diffusion of the particle dominates after times $\tau_K = 6\pi\eta_f R_p/K$. Here R_p refers to the radius of the particle, ρ_p and ρ_f are the mass densities of the particle and the fluid respectively, η_f is the dynamic viscosity of the fluid, and K is the stiffness of the optical trap. R_p may be considered as an effective hydrodynamic radius when the particle is not spherical. The corresponding characteristic frequencies in the Fourier-space can be obtained by: $\Phi_{p,f,K} = 1/2\pi\tau_{p,f,K}$ for all three times. The theoretical PSD along the given direction is given by:

$$\mathrm{PSD}(f) = \frac{D}{\pi^2 f^2}\frac{1+\sqrt{\frac{f}{2\Phi_f}}}{\left(\frac{\Phi_k}{f}-\frac{f}{\Phi_p}-\sqrt{\frac{f}{2\Phi_f}}-\frac{f}{\Phi_f}\right)^2+\left(1+\sqrt{\frac{f}{2\Phi_f}}\right)^2}. \quad (9)$$

Here, D is the diffusion constant, which obeys the Stokes–Einstein equation $D = k_BT/\gamma$, where γ is the coefficient of the instantaneous friction, described by Stokes' law for a sphere: $\gamma = 6\pi R_p\eta_f$.

The MSD along one dimension is calculated as:

$$\begin{aligned}\mathrm{MSD}(t) = 2D\tau_K + \frac{2D}{\tau_p+\frac{\tau_f}{9}}\Bigg[&\frac{e^{z_1^2t}\,\mathrm{erfc}\left(z_1\sqrt{t}\right)}{z_1(z_1-z_2)(z_1-z_3)(z_1-z_4)}\\ &+\frac{e^{z_2^2t}\,\mathrm{erfc}\left(z_2\sqrt{t}\right)}{z_2(z_2-z_1)(z_2-z_3)(z_2-z_4)}\\ &+\frac{e^{z_3^2t}\,\mathrm{erfc}\left(z_3\sqrt{t}\right)}{z_3(z_3-z_1)(z_3-z_2)(z_3-z_4)}\\ &+\frac{e^{z_4^2t}\,\mathrm{erfc}\left(z_4\sqrt{t}\right)}{z_4(z_4-z_1)(z_4-z_2)(z_4-z_3)}\Bigg]. \quad (10)\end{aligned}$$

The four complex roots $(z_1, \ldots, z_4)$ are obtained [20] by solving the polynomial:

$$\left(\tau_p+\frac{\tau_f}{9}\right)z^4-\sqrt{\tau_f}z^3+z^2+\frac{1}{\tau_K}=0. \quad (11)$$

The terms $e^{z_k^2t}\,\mathrm{erfc}$ for $k = 1, \ldots, 4$ in (10) are evaluated for complex numbers with the Faddeeva function [23]:

$$w(z) = e^{-z^2}\,\mathrm{erfc}(-jz) = e^{-z^2}\left(1+\frac{2j}{\sqrt{\pi}\int_0^z e^{t^2}dt}\right). \quad (12)$$

The numerical calculation is performed by the subfunction called 'W.m', provided by Thomas Winiecki [24].

The velocity autocorrelation function reads as:

$$\begin{aligned}\mathrm{VAF}(t) = \frac{k_BT}{m^*}\Bigg[&\frac{z_1^3e^{z_1^2t}\,\mathrm{erfc}\left(z_1\sqrt{t}\right)}{(z_1-z_2)(z_1-z_3)(z_1-z_4)}\\ &+\frac{z_2^3e^{z_2^2t}\,\mathrm{erfc}\left(z_2\sqrt{t}\right)}{(z_2-z_1)(z_2-z_3)(z_2-z_4)}\\ &+\frac{z_3^3e^{z_3^2t}\,\mathrm{erfc}\left(z_3\sqrt{t}\right)}{(z_3-z_1)(z_3-z_2)(z_3-z_4)}\\ &+\frac{z_4^3e^{z_4^2t}\,\mathrm{erfc}\left(z_4\sqrt{t}\right)}{(z_4-z_1)(z_4-z_2)(z_4-z_3)}\Bigg]. \quad (13)\end{aligned}$$

where $m^* = m_p + m_f/2 = 4/3R_p^3\pi(\rho_p+\rho_f/2)$ is the effective mass of the displaced particle and fluid.

Whereas the features of the PSD and MSD curves mostly reflect the characteristics of the diffusive motion and the relaxation by the restoring force, the virtue of the VAF is that the hydrodynamic processes have a discernible effect on the short time behavior of the function, which is already accessible in high-resolution optical trapping experiments [22]. Due to the backflow of the displaced fluid, the correlations in the velocity of the particle are prolonged, resulting in a power-law character – often referred to as a long-time tail – as opposed to an exponential decay [25]. Therefore the short time regime of the VAF becomes highly sensitive to the properties of the fluid, allowing for local microrheologic measurements [19]. Other distinguishable features such as the arising anticorrelations in the VAF due to the restoring force of the trap, and the corresponding turning points in the PSD and the MSD provide sufficient information for the accurate calibration of the optical tweezers even without prior knowledge of the radius of the captured bead [26]. We exploit these attributes to find a reliable initialization point for the calibration parameters before the full-scale fitting.

3.2. Rotational Brownian motion

When evaluating the contribution of the rotational fluctuations to the detected signal, we follow the approximations proposed by Marago [13], and neglect the inertial effects of both the particle and the fluid. However, depending on the sensitivity of the detector to the rotation ($\alpha_{i\Theta}$), corrections may be necessary due to the hydrodynamic memory effects arising upon the rotation of the particle, in particular at high frequencies and short times. In this simplified model, only rotational diffusion is considered, confined by the restoring torque of the trap. Correspondingly, the PSD is described by an overdamped Lorentzian, whereas the MSD and the VAF perform an exponential relaxation, as follows:

$$\mathrm{PSD}_\Theta(f) = \frac{D_\Theta}{\pi^2 f^2\left(1+\left(\frac{\Phi_\Theta}{f}\right)^2\right)} \quad (14)$$

$$\mathrm{MSD}_\Theta(t) = 2D_\Theta\tau_\Theta(1-e^{-t/\tau_\Theta}) \quad (15)$$

$$\mathrm{VAF}_\Theta(t) = -2D_\Theta/\tau_\Theta e^{-t/\tau_\Theta}, \quad (16)$$

where D_Θ is the rotational diffusion constant, τ_Θ is the timescale associated to the rotational relaxation due to the restoring torque

and $\Phi_\Theta = 1/2\pi\tau_\Theta$ is the corresponding corner frequency. Even though there is an overall scaling factor, $\beta_{ii}^2\alpha_{i\Theta}^2$ emerging in the rotational terms of (6)–(8), this appears exactly in the same role as D_Θ, and therefore they are not distinguishable by fitting. Consequently, we introduce two independent parameters describing the rotational terms in the PSD, the MSD and the VAF. A convenient choice is to select the uncalibrated saturation values (that is the $f \to 0$ and $t \to \infty$ limits) of the rotational PSD and MSD, containing the product of the rotational diffusion constant and sensitivity values: $\mathrm{MSD_{rot}} = 2D_\Theta\tau_\Theta\alpha_{i\Theta}^2$ and $\mathrm{PSD_{rot}} = \alpha_{i\Theta}^2 D_\Theta/\pi^2\Phi_\Theta = 4\alpha_{i\Theta}^2 D_\Theta\tau_\Theta$. These values can be easily read off the graphs to obtain good initialization points. Expressing D_Θ, τ_Θ and Φ_Θ parameters in terms of the definitions of $\mathrm{PSD_{rot}}$ and $\mathrm{MSD_{rot}}$, Eqs. (14)–(16) can be evaluated.

4. Fitting parameters

The following independent parameters are required to calculate the PSD, MSD and VAF curves, and to perform the fitting along one direction:

1. R_p (μm): Particle radius or equivalent hydrodynamic radius, if not spherical.
2. K (μN/m): Stiffness of the optical trap.
3. β^2 ($\mathrm{nm^2/V^2}$): Translational voltage-to-displacement factor (inverse sensitivity of the detector) squared.
4. $\mathrm{PSD_{rot}}$ ($\mathrm{V^2/Hz}$): Low-frequency plateau value of the rotational PSD measured by the detector.
5. $\mathrm{MSD_{rot}}$ ($\mathrm{V^2}$): Long-time plateau value of the rotational MSD measured by the detector.
6. ρ_p ($\mathrm{kg/m^3}$): Mass density of the particle.
7. ρ_f ($\mathrm{kg/m^3}$): Mass density of the surrounding fluid.
8. η_f (mPas): Dynamic viscosity of the fluid.
9. T (K): Temperature of the fluid.

In the current version of the calibration program one can obtain parameters 1–5 by fitting, while parameters 6–9 must be set corresponding to the measurement conditions. When the probe is spherical, 'Spherical' option should be checked to remove the rotational terms from the model, thus only parameters 1–3 are returned by the fitting. By applying the 'Non-Spherical' option, the rotational contributions will be added to the fitted functions, yielding values for parameters 4 and 5. Note, that it is possible to fix the value of any of the parameters above, if they are known in the experiment. When the exact size and shape of the probe are known, the rotational diffusion constant D_Θ can be computed, hence the rotational sensitivity $\alpha_{i\Theta}$ of the detection system and the torsional spring constant $k_\Theta = D_\Theta/k_B T\tau_\Theta$ can be inferred from the fitted parameters 4 and 5.

5. Preprocessing experimental data

The calibration program allows for the simultaneous fitting of the PSD, MSD and VAF curves. The values of the three functions however extend over several orders of magnitude. Thus prior to performing a least-square type fitting algorithm, the respective function values must be normalized to a common scale in order to avoid bias towards the highest function values. Two possible solutions emerge. The exponential and power-law character of the statistical functions offers their logarithmic transformation to the common [0 1] range:

$$y_\mathrm{log} = \frac{1}{B}\ln(y/A), \tag{17}$$

where $A = \max(y)$, $B = \min(\ln(y/A))$, and y corresponds to the measured values of the $\mathrm{PSD^{exp}}$, $\mathrm{MSD^{exp}}$ or $\mathrm{VAF^{exp}}$. If there are Δy error values assigned to the data points, they are transformed accordingly:

$$\Delta y_\mathrm{log} = \frac{1}{B}\frac{\Delta y}{y}. \tag{18}$$

This transformation is performed on the data and the theoretical functions prior to fitting if the 'Logarithmic transformation' option under 'Fitting Options' menu is selected. If the 'Linear' option is chosen, the data will not be subject to the above transformation.

Another solution is offered when error to the measured data has been estimated. The variance of the measured observables is not uniform, therefore weighted least squares provide the best quantity to be minimized by the fitting:

$$\chi^2 = \sum_{j=1}^{N}\left(\frac{y_j - f(x_j)}{\Delta y_j}\right)^2 = \min, \tag{19}$$

where Δy_j is the estimated error to the individual data points, y_j refers to the jth measurement point of $\mathrm{PSD^{exp}}$, $\mathrm{MSD^{exp}}$ or $\mathrm{VAF^{exp}}$, $f(x_j)$ is the fitted value of the corresponding function. Whenever 'Linear' option is selected, weighting is automatically performed prior to submission to the least-square fitting algorithm:

$$\begin{aligned}\mathrm{PSD}_w^\mathrm{exp} &= \mathrm{PSD^{exp}}/\Delta\mathrm{PSD},\\ \mathrm{MSD}_w^\mathrm{exp} &= \mathrm{MSD^{exp}}/\Delta\mathrm{MSD},\\ \mathrm{VAF}_w^\mathrm{exp} &= \mathrm{VAF^{exp}}/\Delta\mathrm{VAF},\end{aligned} \tag{20}$$

where the lower w index denotes weighted data.

6. Using the software

In this section, we introduce the different functions of the software following the order dictated by a general calibration task.

6.1. Starting the program

To run the calibration program, the user must load 'PFMCal.m' in MatLab and click on run or type 'PFMCal' in the main terminal. The path should be added to MatLab or the current directory must be changed accordingly.

6.2. Selecting data to fit

The user can load the $\mathrm{PSD^{exp}}$, $\mathrm{MSD^{exp}}$ and $\mathrm{VAF^{exp}}$ data distributed in three columns (x, y, err), by clicking on the 'load PSD', 'load MSD', and 'load VAF' buttons respectively (see Fig. 1). It is not necessary to load all the three functions, but it is recommended in order to increase fitting performance. The loaded data can be visualized by clicking on the 'Plot with actual parameters' button shown in Fig. 2.

6.3. Fitting options menu

The user can customize various settings of the fitting (Fig. 2(a)) to achieve the best performance. The main options are the following:

- Model select: The user can choose between 'Spherical' and 'Non-spherical' models as described in Sections 3.1 and 3.2.
- Transformation: The user can select between linear or logarithmic transformation (see Section 5).
- Functions to fit: The user can define, which functions out of the PSD, MSD and VAF should be fitted by the algorithm. Fitting all three functions simultaneously may improve efficiency. By unchecking all, the software will return the values of the initialization points, without performing least-square fitting.

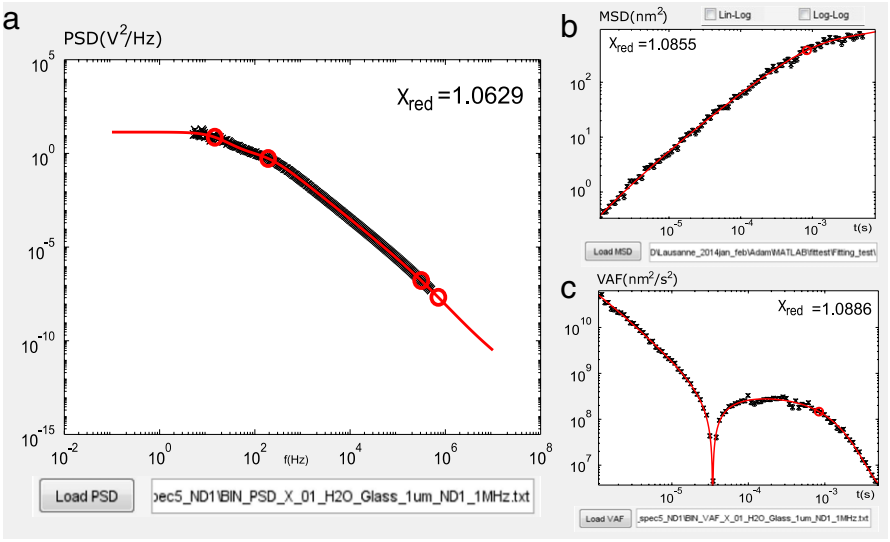

Fig. 1. Loading and plotting of the (a) PSD (magnified), (b) MSD and (c) VAF data in the graphical user interface. Measured data points are represented by black crosses with error bars, fitted functions are displayed with red curves. Red circles show characteristic frequencies and time scales. Reduced chi-square values of the actual fitting are displayed inside the plot area.

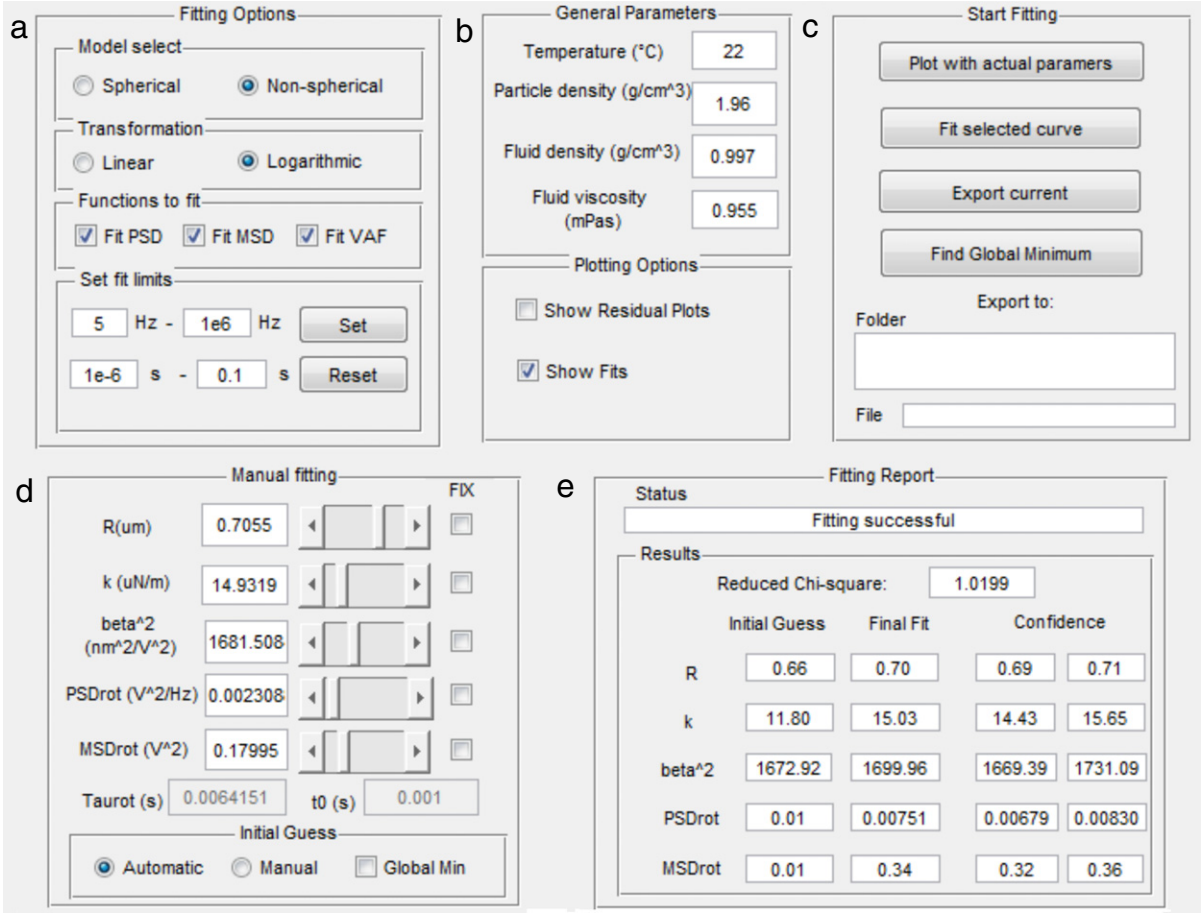

Fig. 2. Fitting option panels in the graphical user interface. The layout of the user interface is rearranged in the figure for the sake of better visibility.

- Set fit limits: The user can select the fitting range for each dataset. Values are defined in Hz for the PSD, and in seconds for the MSD and VAF. The selected limits can be activated and the cropped data is displayed upon clicking on 'Set' button. The original data can be restored by clicking on the 'Reset' button.

6.4. General parameters menu

The user must specify the constant parameters describing the measurement conditions as follows (Fig. 2(b)):

- Temperature of the fluid in degree Celsius.
- Density of the particle in g/cm^3.

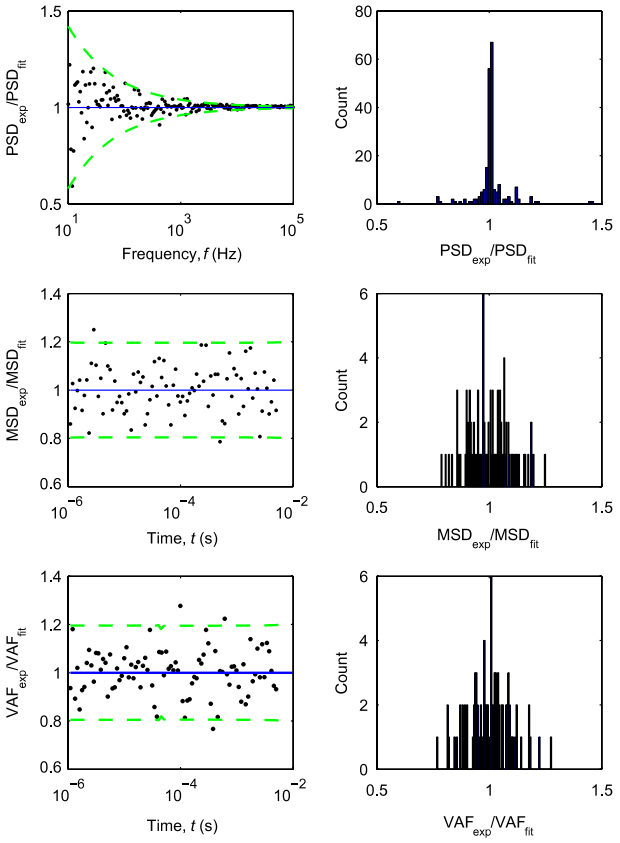

Fig. 3. Graphs in the left column display the relative residual errors, i.e. the ratio of the experimental points and the fitted curves, represented by black dots. Solid blue lines indicate unity, the value for a perfect fit, which serves as a guide to the eye. Green dashed lines show the 95% confidence intervals for the normally distributed data points with the corresponding errors. For the custom generated data plotted here, a uniform 10% error was chosen for the MSD and the VAF (middle and bottom rows). In case of the PSD (top row), where logarithmic binning was simulated, the error decreases with the square root of the number of binned data points per bin. Figures in the right column show the distribution histograms of the relative residuals. In the software the arrangement of the graphs is transposed.

- Density of the fluid in g/cm^3.
- Viscosity of the fluid in mPas.

6.5. Plotting options menu

- Show Residual Plots: Checking this box will allow the 'Residual plots' window to pop up upon fitting (see Fig. 3).
- Show Fits: The fitted curves will appear in a separate window (Fig. 4).

6.6. Manual fitting menu

In this menu (Fig. 2(d)), the user can manually customize the parameter values and observe the theoretical curves change accordingly in real time. This is also where the user may manually set the initialization points for the parameters, by choosing between 'Manual' and 'Automatic' options. By checking 'Global minimum' option, the program will perform multiple fitting procedures started from different initial points and select the fit with the lowest chi-square value in order to avoid convergence to a local minimum. This action may take extended time.

The parameters can be fixed by checking the corresponding boxes under the label 'Fix'.

6.7. Start fitting menu

This menu (Fig. 2(c)) allows the user to perform the fitting with all the previously selected options and to plot the current results.

- Plot with actual parameters: Theoretical curves and data points are plotted using the parameters set in the 'Manual fitting' menu. Note, that plotting with this button renders each fitted function with 1000 data points, whereas setting the parameters manually and moving the sliders uses only 100 points to ensure rapid visualization and quick response.
- Fit selected curve: Fitting is performed with the previously selected options.
- Export current: Upon clicking on this button, the software saves all the fitting parameters to a file specified by the user. The calculated PSD, MSD and VAF curves together with the original data points are saved in a .txt file for later manipulation and custom plotting. The software prompts the user to select the destination using a file explorer.
- Find global minimum: A global minimum search is performed, by varying the initial guesses for the parameters, and fitting each sets. The algorithm will select and render the result with the lowest residual.

6.8. Fitting report menu

In this menu (Fig. 2(e)) the user can follow the results of the fitting procedure. The status textbox provides information about the status of fitting. In the Results box, the program displays the results of fitting. This involves the initialization points of the parameters, the final fitted values, and the 95% confidence ranges returned by the algorithm.

7. Testing and application

The performance of the software was tested on computer generated data as well as on experimental data.

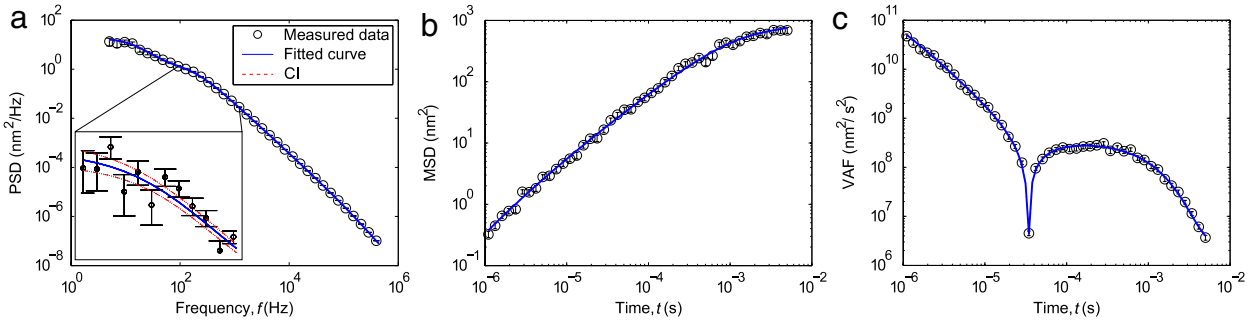

Fig. 4. When the 'Show fits' option is checked, the fitted curves are displayed (solid blue line) with the predicted 95% confidence intervals (red dotted line) on the top of the measured data (black circles with error bars) for (a) the PSD, (b) MSD and (c) VAF. The inset in the PSD figure contains a zoomed image of the PSD plot.

7.1. Test results on computer generated data

Test data were produced by generating typical PSD, MSD and VAF curves comprising 270, 90 and 90 data points, respectively, using the non-spherical model (9)–(16) with chosen input parameters. In order to simulate the noise of the measurement and the effect of the subsequent binning procedure and error estimation, a non-uniform noise was added to the statistical functions.

For simplicity, the standard deviation of the original data points was assumed to be proportional to their expectation value, i.e. the relative standard deviation, σ_y/y to be constant. In theory, this constant factor is exactly 1 for the PSD, being an exponentially distributed probability variable [8]. In order to test logarithmic binning, $n = 30$ bins/decade spacing was selected in the case of the PSD, where the number of data points per bin are given by: $N_b(f) = T_{\text{meas}} * (10^{1/n} - 1) f$. Here, f denotes the central frequency of the corresponding block and $T_{\text{meas}} = 30$ s was used as the typical acquisition time of a single measurement. After all, the noise of the PSD was synthesized by normally distributed random number generation with zero expectation value and $\Delta\text{PSD}(f) = \text{PSD}(f)/\sqrt{N_b(f)}$ standard deviation for the logarithmically spaced points in the frequency range. At the same time, a uniform binning, corresponding to a uniform relative error was assigned to the MSD and the VAF, chosen arbitrarily to be 10%: $\Delta\text{MSD}(t) = 0.1 * \text{MSD}(t)$, $\Delta\text{VAF}(t) = 0.1 * \text{VAF}(t)$. The input parameters for the synthetic data were the following:

$R_p = 0.7\ \mu\text{m}$
$K = 15\ \mu\text{N/m}$
$\beta^2 = 1700\ \text{nm}^2/\text{V}^2$
$\text{PSD}_{\text{rot}} = 0.008\ \text{V}^2/\text{Hz}$
$\text{MSD}_{\text{rot}} = 0.36\ \text{V}^2$.

The last two parameters were used for the simulation the additional rotational fluctuations (14)–(16). We applied the physical properties of silica and water at $T = 22\ ^\circ\text{C}$ to simulate experimental conditions identical to the real measurements described in the following section: $\rho_p = 1.96\ \text{g/cm}^3$, $\rho_f = 0.997\ \text{g/cm}^3$, $\eta_f = 0.955$ mPas.

100 datasets were generated with the same input parameters but random additional noise. All datasets were fitted by each fitting option to test the distribution of the fitted parameters (shown in Fig. 5). The best performance was achieved in the linear option, where the functions and input data were left untransformed, and were weighted by the error values. The fitted parameters scatter around the real values and the obtained 95% confidence intervals predict well the actual standard deviation of the results (confidence intervals not shown). In case of the logarithmic transformation without weighting, the fitting converges to multiple discrete points around the real value (red histogram), which implies that new local minima are introduced by the nonlinear transformation. Using the global minimum search option (blue histogram) highly improves the results. The parameter estimates are not biased, though the standard deviation of the fitted values is somewhat larger than that in the linear mode. The advantage of the logarithmic transformation is that the fitting can converge without weighting, which makes it possible to fit data even when no errors were previously estimated. All other fitted parameters follow similar distributions and are thus not shown here.

7.2. Test results on measured data

Test measurements were performed with custom-made optical tweezers [27] utilizing a diode-pumped Gaussian beam, ultra-low noise Nd:YAG laser with a wavelength of $\lambda = 1064$ nm, and a maximal light power of 500 mW in continuous wave mode (IRCL-500-1064-S, CrystaLaser, USA). The trapping light was focused by a high numerical aperture (NA = 1.2), 60x water-immersion objective (UPLapo/IR,Olympus, Japan). The position detection was achieved by an InGaAs quadrant photodiode with an active area of 2 mm in diameter (QPD, G6849, Hamamatsu Photonics, Japan). Data were collected by a data acquisition board with a dynamic range of 12 bits (NI-6110, National Instruments, USA) at 1 MHz sampling rate. The cutoff of the amplification system at the maximal gain of 500 was around 1 MHz. The PSD^{exp}, MSD^{exp} and VAF^{exp} data were calculated by a custom-designed program.

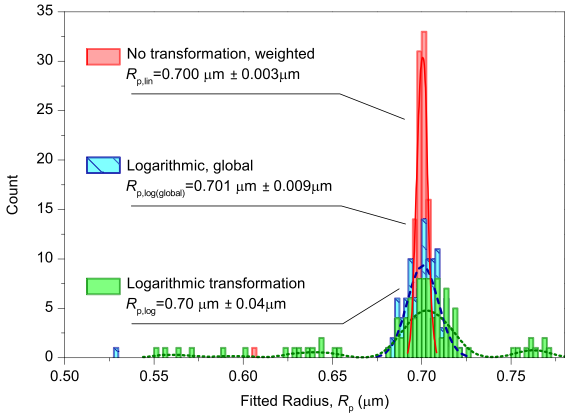

Fig. 5. Distribution of the fitted radius, R_p, for the synthetic data using three different fitting options. Red, green and blue (striped) colors represent 'Linear', 'Logarithmic' and 'Logarithmic' together with 'Global minimum' options, respectively. The fitted curves on the top of the histograms are guides to the eye (solid, dotted and dashed lines with the same color coding). The real radius was $R_p = 0.7$ μm. The mean and the standard deviation of the 100 fittings are summarized in the legend for each option. (For interpretation of the references to color in this figure legend, the reader is referred to the web version of this article.)

Silica spheres were used to test the 'Spherical' fitting option (Fig. 6(d)). The bead radius is known from the manufacturer to be 0.505 μm within 4% tolerance. The physical parameters were the following: $\rho_p = 1.96\ \text{g/cm}^3$, $\rho_f = 0.997\ \text{g/cm}^3$, $\eta_f = 0.955$ mPas, the measurement was performed at $T = 22\ ^\circ\text{C}$. The fitting range was confined to $5\text{–}10^5$ Hz in order to exclude low-frequency noise and aliasing effects close to the sampling frequency. In case of the linear mode fitting, a temporal range of $t = 10^{-6}\text{–}10^{-2}$ s was set to avoid bias in the estimated errors due to long-time correlations in the MSD and VAF functions. The obtained parameters in the different fitting modes are summarized in Table 1 and the fitted functions are displayed in Fig. 6(a)–(c). The parameters are in good agreement in the two modes, and the estimated radius corresponds well to the nominal radius of the bead.

In order to investigate the Brownian motion of a randomly shaped object, larger silica spheres of 100 μm diameter were crushed in a mortar to 1–2 μm sized, randomly shaped particles, one of which was captured by the optical trap (Fig. 6(h)). The appearance of a second plateau can be seen in the PSD (Fig. 6(e)), which can be readily fitted by the non-spherical model. The same fitting ranges were used as in the case of the spherical probe. Table 1 contains the fitted parameters and the corresponding curves are shown in Fig. 6(e)–(g). The parameters and the fits show good consistency in the two different modes, supporting the use of the non-spherical model.

In order to demonstrate the robustness of the methodology, the automated fitting procedure has been executed using experimental data from a series of consecutive measurements on a single polystyrene sphere in the optical trap. The nominal radius of the bead was 0.74 μm with a density of $\rho_p = 1.05\ \text{g/cm}^3$. The polarization direction of the trapping laser was rotated in 20° steps

Table 1
Comparison of the fitting parameters obtained for a spherical silica bead as well as a non-spherical silica particle using different fitting options.

Probe	Mode	Range f (Hz)	Range t (s)	R_p (μm)	k (μN/m)	β^2 (nm^2/V^2)
Spherical	Lin	5–10^5	10^{-6}–10^{-3}	0.500 ± 0.005	8.2 ± 0.2	1640 ± 25
	Log	5–10^5	10^{-6}–10^{-2}	0.5 ± 0.1	8.2 ± 0.5	1550 ± 70
Non-spherical	Lin	5–10^5	10^{-6}–10^{-3}	0.73 ± 0.03	16 ± 1	1750 ± 25
	Log	5–10^5	10^{-6}–10^{-2}	0.72 ± 0.03	15 ± 1	1700 ± 70

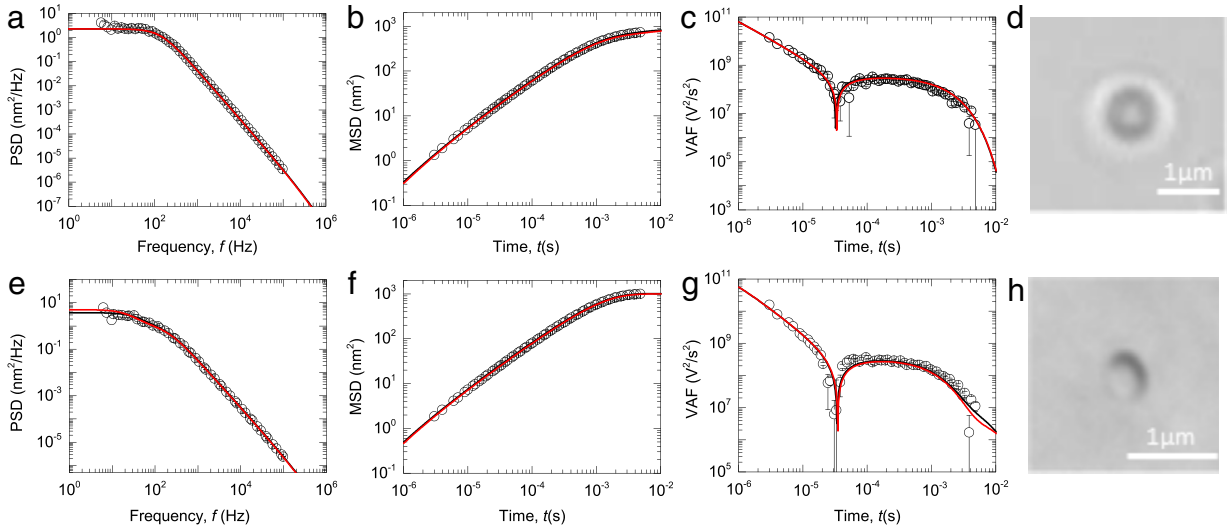

Fig. 6. Fitting results for the PSD MSD and VAF experimental data measured on a $R_p = 0.505$ μm diameter silica sphere captured in the trap (top row, (a)–(c)), as well as on a non-spherical silica probe (bottom row, (e)–(g)). Black circles indicate experimental points. Black fitted curves were obtained using the 'Linear fitting' option, whereas red curves show the result of fitting with 'Logarithmic transformation' option. CCD camera images of the captured probes are displayed in the fourth column (d) and (h). White bars indicate 1 μm length. (For interpretation of the references to color in this figure legend, the reader is referred to the web version of this article.)

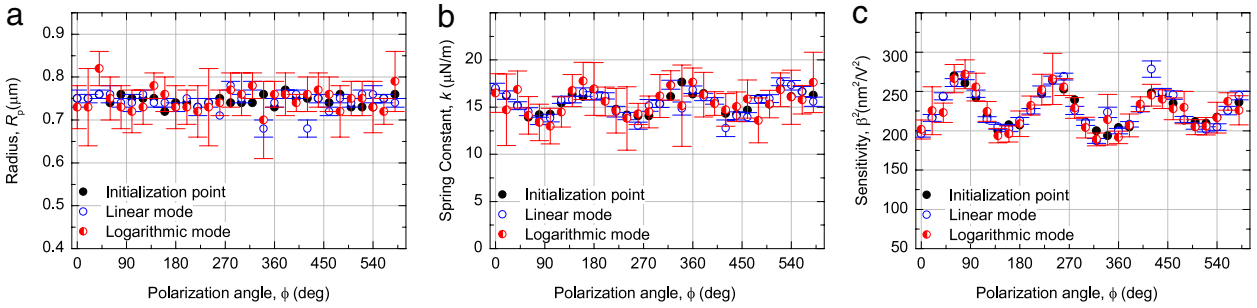

Fig. 7. Obtained fitting parameters (radius: (a), trap stiffness: (b) and detector sensitivity: (c)) in the function of the polarization angle of the trapping laser. The initialization points are displayed by black dots. Blue circles and half-filled red circles indicate parameters yielded by the linear and logarithmic fitting mode, respectively. Error bars represent the associated 95% confidence intervals obtained by the fitting algorithm.

between measurements up to more than one and a half full cycle (560°). Fitting ranges were set to $t = 10^{-6}$–10^{-3} s and $f = 100$–10^5 Hz. Fig. 7 displays the fitting results for all polarization angles, ϕ. The radius of the bead is estimated accurately both in the linear (blue dots) and the logarithmic mode (red dots). Moreover, the initialization points (black dots) also provide a very good approximation of the real radius, meaning that the characteristic features of the MSD and VAF curves – which define the initial parameters – are robust enough to be measured and determined with high accuracy.

Upon the rotation of the polarization of the trapping light, the obtained spring constant and sensitivity values (Fig. 7(b) and (c)) are periodically modulated with a periodicity of 180°. The modulation of the trap stiffness originates from the polarization induced asymmetry in the trapping potential. Furthermore, a change in the laser intensity arises if there is any polarizing elements in the light path, resulting in a modulation of both the trap stiffness and the detector sensitivity. The fitted parameters show very good consistency and reproducibility, which confirms the applicability of the software.

8. Conclusion

We have developed a calibration software for optical tweezers based on the Brownian motion of the probe, sampled with high frequency. In our model we employ the proper hydrodynamic theory for the PSD, MSD and VAF, as well as a qualitative extension for handling rotational fluctuations, or alternatively any additional relaxation processes involved in the dynamics of the particle. The software was tested for synthetic and experimental data. The results confirmed the applicability of the software. It is important to note that since the linear mode performs weighting by errors, a correct error estimation of the input data is crucial, which is not always straightforward for correlated data [16]. The logarithmic

mode on the other hand not only removes the orders-of-magnitudes difference between data values but also makes noise more uniform, which enhances the performance of optimization by unweighted least squares, meaning that no prior error estimation is needed. This flexibility comes at a price of losing the information of the variance in the presence of heteroscedasticity. Consequently, whereas the parameter estimates remain unbiased in the logarithmic mode, they could be further optimized by adequate weighting, as demonstrated by the results on synthetic data. The possible selection between the two fitting modes allows the user to adapt to the properties of the experimental data at hand.

Acknowledgments

A.B. was supported by the Hungarian Research Funds, OTKA K 108918. F.M.M. acknowledges support from the National Centre of Competence in Research (NCCR Nano-Bio, Project 1.4) and the Swiss National Science Foundation (SNSF, Project numbers 206021_121396 and 200021_143703). F.M.M. was supported by the National Competence Center in Biomedical Imaging (NCCBI). P.D.G acknowledges M.E.C.D. for financial aid by project FIS2013-47350-C5-5-R.

Appendix. List of program subroutines

Program subroutines are categorized function-wise, structured into a directory-tree.

A.1. PFMCal.m

This is the main function of the program. It contains the initialization and object declaration commands. No functional part of the program is included here. In order to start the graphical user interface, the user must start this function in MatLab either from the command line or by clicking on 'Run' in the editor window. PFMCal.fig is the corresponding MatLab GUI file.

A.2. Button actions

Functions located in this folder respond to the user clicking on the main buttons on the user interface. Actions include loading measured data, manual parameter and fitting settings as well as main procedures, such as fitting, plotting, saving. The MatLab functions can be found in subdirectories corresponding to the enumerated elements below:

1. Fitting settings: Handles the options selected in the 'Fitting Options Menu' (see Section 6.3). List of functions:
   - automatic_initguess_Callback.m: Selection between automatic and manual initial guess. Selecting 'Automatic' switches the 'Manual' option off.
   - manual_initguess_Callback.m: Selection between an automatic or a manual initial guess. Selecting 'Manual' switches the 'Automatic' option off.
   - single_Callback.m: Selection between spherical and non-spherical fitting model. This function switches the 'Non-spherical' option off.
   - double_Callback.m: Selection between spherical and non-spherical fitting model. This function switches the 'Spherical' option off.
   - linear_Callback.m: Selection between linear and logarithmic transformation of measurement data. Selecting 'Linear' switches the 'Logarithmic' option off.
   - logarithmic_Callback.m: Selection between linear and logarithmic transformation of data. Selecting 'Logarithmic' switches the 'Linear' option off.
2. Load_data: Functions in this directory manage the import of data (PSD, MSD and VAF) by clicking on the corresponding button or changing the access path.
   - loadpsd_Callback.m: Opens a file explorer to locate the PSD^{exp} file.
   - loadMSD_Callback.m: Opens a file explorer to locate the MSD^{exp} file.
   - loadVAF_Callback.m: Opens a file explorer to locate the VAF^{exp} file.
   - psdpath_Callback.m: Reads the PSD^{exp} file from the typed path.
   - msdpath_Callback.m: Reads the MSD^{exp} file from the typed path.
   - vafpath_Callback.m: Reads the VAF^{exp} file from the typed path.
   - Set_Callback.m: Crops experimental PSD^{exp}, MSD^{exp} and VAF^{exp} according to the intervals added in 'Set Fit Limits' menu. Uses: Calculate_Callback and Plot_Callback.
   - Reset_Callback.m: Restores original experimental PSD^{exp}, MSD^{exp} and VAF^{exp} data from the respective data files.
   - Clearall_Callback.m: Clears experimental PSD^{exp}, MSD^{exp} and VAF^{exp} data and the corresponding graphs.
3. Manual Parameter Settings: Calculates the PSD, MSD and VAF functions upon setting the parameters manually, either by typing in the boxes or by moving the corresponding sliders next to the parameter boxes. All functions incorporate the Calculate_Callback.m and Plot_Callback.m functions located in the 'Calculatefn' and 'Plotting' folders, respectively.
   - as_Callback.m: Refreshes the graphs after changing the radius parameter.
   - aslider_Callback.m: Refreshes the graphs after changing the radius parameter by moving the slider.
   - k_Callback.m: Refreshes the graphs after changing the spring constant parameter.
   - kslider_Callback.m: Refreshes the graphs after changing the spring constant parameter by moving the slider.
   - b_Callback.m: Refreshes the graphs after changing the sensitivity parameter.
   - bslider_Callback.m: Refreshes the graphs after changing the sensitivity parameter by moving the slider.
   - PSDmax_Callback.m: Refreshes the graphs after changing the PSD second plateau value parameter.
   - PSDslider_Callback.m: Refreshes the graphs after changing the PSD second plateau value parameter by moving the slider.
   - MSDmax_Callback.m: Refreshes the graphs after changing the MSD second plateau value parameter.
   - MSDslider_Callback.m: Refreshes the graphs after changing the MSD second plateau value parameter by moving the slider.
4. Main_actions: The functions located here perform the main actions to the corresponding button clicks.
   - Plot_with_actual_parameters_Callback.m: Performs plotting with the parameters and options set by the user. Uses: Calculate_Callback.m, and Plot_Callback.m.
   - Fit_selected_curve_Callback.m: Performs the fitting as defined by the selected fitting options.
     Uses: Initialguess_Callback.m, MaxLikelihood_Callback.m, Calculate_Callback.m, Plot_Callback.m.
   - Export_current_Callback.m: Exports the current fits including the PSD^{exp}, MSD^{exp} and VAF^{exp} data, graphs and fitting parameters into specified folder and output files. Uses: plot_hold.m.
   - Find_global_min_Callback.m: Starts the least-square fitting algorithm from a 2D-grid of different radius and spring constant parameters as initialization points to find convergence to a lower minimum. Uses: MaxLikelihood_Callback.m.

A.3. Calculatefn

The functions in this folder are associated to the calculation of the theoretical PSD, MSD and VAF functions. PSDdouble.m, MSDdouble.m and VAFdouble.m are the only functions responsible for the description of the theoretical model. Any modification to the model functions should be incorporated in these functions.

- Calculate_Callback.m: Calculates the necessary quantities and the PSD, MSD and VAF functions from the input parameters read from the GUI. Uses: PSDdouble.m, MSDdouble.m, VAFdouble.m, W.m.
- PSDdouble.m: Contains the theoretical function for the PSD curve with translational and rotational components. Characteristic frequencies are passed through the parameter list of the function.
- MSDdouble.m: Contains the theoretical function for the MSD curve with translational and rotational components. Characteristic time scales are passed through the parameter list of the function. Uses: W.m.
- VAFdouble.m: Contains the theoretical function for the VAF curve with translational and rotational components. Characteristic time scales are passed through the parameter list of the function. Uses: W.m.
- psdmsdvaf_single.m: Calculates the translational PSD, MSD and VAF functions. Uses: W.m.
- W.m: Numerical evaluation of the Faddeeva function [24].

A.4. Preprocessing data

Functions in this directory are necessary for the transformation of the data and the fitted theoretical function as described in Section 5.

- preprocess.m: Reads the input data, denoted as psdx, msdx and vafx, and concatenates them into one array. Performs logarithmic transformation on the data if selected by the user. The function also returns the length of the PSD, MSD and VAF datasets for their later separation.
- modelfunction.m: This function provides the theoretical functions for the fitting procedure. The PSD, MSD and VAF functions are calculated by PSDdouble.m, MSDdouble.m and VAFdouble.m and logarithmic transformation is performed subsequently, if this option is selected. The three functions are concatenated to be compatible with the experimental data.

A.5. Fitting

This directory contains the functions necessary for the fitting procedure.

1. Initial Guess: Contains functions for providing accurate initialization points for the least-square fitting procedure. The initial guess algorithm is based on the paper by Grimm et al. [26]. After an initial radius is assumed, a guess on the spring constant is obtained by finding the zero-crossing of the VAF, then the sensitivity (β^2_{VAF}) is estimated by aligning the theoretical curve to the VAF data points. Simultaneously, a sensitivity value is inferred from the MSD amplitude β^2_{MSD}. The two different β^2 values are compared and the initial radius is varied iteratively until the two values agree within a given tolerance. This fixes the initial radius $R_{p,0}$ and the sensitivity β^2_0 values. Finally the spring constant k_0 is refined stepwise until the MSD turning point follows perfectly the data points. PSD_{rot} and MSD_{rot} values are respectively calculated from the difference between the maximum of the experimental PSD^{exp} and MSD^{exp} data points and the plateau value of the translational terms (Eqs. (9) and (10)) estimated from the initial $R_{p,0}$, β^2_0 and k_0 parameters.
   - Initialguess_Callback.m: Starts the initial guessing procedure with the options set by the user on the GUI. Uses: fit_singleplateau.m.
   - fit_singleplateau.m: Manages the initial guess procedure using the following subroutines: t0VAF.m, psdmsdvaf_single.m, betaVAF.m, betaVAF_equals_betaMSD.m, refine_kMSD.m.
   - t0VAF.m: Finds the zero-crossing of the VAF and calculates the corresponding spring constant. Uses t0Tauf.mat.
   - betaVAF.m: Calculates the sensitivity for the VAF.
   - betaVAF_equals_betaMSD.m: Tests exit conditions for the iteration. When the two sensitivity values agree within a tolerance, the radius and the sensitivity is accepted.
   - refine_kMSD.m: Refinement of the spring constant.
   - maxvalues.m: Finds maximal values of PSD and MSD to obtain a guess for PSD_{rot} and MSD_{rot}.
   - t0Tauf.mat: Table for the calculation of the spring constant from the zero-crossing of VAF.
2. Maximum Likelihood: Functions in this folder perform the maximum likelihood fitting of the theoretical functions to the measurement data.
   - MaxLikelihood_Callback.m: Processes the fitting options set by the user, and initializes the fitting algorithm accordingly, then displays the results on the GUI. Uses: MLHdouble.m, showfits.m.
   - MLHdouble.m: Performs least-square fitting with optional weighting of the data points. Uses: preprocess.m, modelfunction.m. MatLab functions required for the fitting procedure: `nlinfit` and `nlpredci` are included in the Statistics Toolbox. Passes the obtained parameters and respective confidence intervals back to the calling function.

A.6. Plotting

All the functions required for the plotting are collected in this directory.

- Plot_Callback.m: Performs plotting on the main GUI axes according to the selected options.
- plot_hold.m: Plots exportable graphs upon pushing the 'Export current fit' button.
- showfits.m: Plots fits and predicted confidence intervals if the 'Show fit' checkbox is selected.

References

[1] A. Ashkin, Acceleration and trapping of particles by radiation pressure, Phys. Rev. Lett. 24 (4) (1970) 156.
[2] S. Keen, J. Leach, G. Gibson, M. Padgett, Comparison of a high-speed camera and a quadrant detector for measuring displacements in optical tweezers, J. Opt. A: Pure Appl. Opt. 9 (8) (2007) S264.
[3] K. Svoboda, S.M. Block, Biological applications of optical forces, Annu. Rev. Biophys. Biomol. Struct. 23 (1) (1994) 247–285.
[4] M.W. Allersma, F. Gittes, R.J. Stewart, C.F. Schmidt, et al., Two-dimensional tracking of ncd motility by back focal plane interferometry, Biophys. J. 74 (2) (1998) 1074–1085.
[5] F. Gittes, C.F. Schmidt, Interference model for back-focal-plane displacement detection in optical tweezers, Opt. Lett. 23 (1) (1998) 7–9.
[6] A. Pralle, M. Prummer, E.-L. Florin, E. Stelzer, J. Hörber, et al., Three-dimensional high-resolution particle tracking for optical tweezers by forward scattered light, Microsc. Res. Tech. 44 (5) (1999) 378–386.
[7] I.M. Tolić-Nørrelykke, K. Berg-Sørensen, H. Flyvbjerg, Matlab program for precision calibration of optical tweezers, Comput. Phys. Comm. 159 (3) (2004) 225–240.
[8] K. Berg-Sørensen, H. Flyvbjerg, Power spectrum analysis for optical tweezers, Rev. Sci. Instrum. 75 (3) (2004) 594–612.
[9] F.M. Mor, A. Sienkiewicz, L. Forró, S. Jeney, Upconversion particle as a local luminescent Brownian probe: A photonic force microscopy study, ACS Photonics 1 (12) (2014) 1251–1257.
[10] O.M. Maragó, F. Bonaccorso, R. Saija, G. Privitera, P.G. Gucciardi, M.A. Iatì, G. Calogero, P.H. Jones, F. Borghese, P. Denti, et al., Brownian motion of graphene, ACS Nano 4 (12) (2010) 7515–7523.
[11] H. Zhang, K.-K. Liu, Optical tweezers for single cells, J. R. Soc. Interface 5 (24) (2008) 671–690.

[12] H. Kress, E.H. Stelzer, A. Rohrbach, Tilt angle dependent three-dimensional-position detection of a trapped cylindrical particle in a focused laser beam, Appl. Phys. Lett. 84 (21) (2004) 4271–4273.
[13] O. Marago, P. Jones, F. Bonaccorso, V. Scardaci, P. Gucciardi, A. Rozhin, A. Ferrari, Femtonewton force sensing with optically trapped nanotubes, Nano Lett. 8 (10) (2008) 3211–3216.
[14] M. Grießhammer, A. Rohrbach, 5d-tracking of a nanorod in a focused laser beam-a theoretical concept, Opt. Express. 22 (5) (2014) 6114–6132.
[15] A.A. Bui, A.B. Stilgoe, T.A. Nieminen, H. Rubinsztein-Dunlop, Calibration of nonspherical particles in optical tweezers using only position measurement, Opt. Lett. 38 (8) (2013) 1244–1246.
[16] H. Flyvbjerg, H.G. Petersen, Error estimates on averages of correlated data, J. Chem. Phys. 91 (1) (1989) 461–466.
[17] M. Capitanio, G. Romano, R. Ballerini, M. Giuntini, F. Pavone, D. Dunlap, L. Finzi, Calibration of optical tweezers with differential interference contrast signals, Rev. Sci. Instrum. 73 (4) (2002) 1687–1696.
[18] F.M. Mor, Developing luminescent Brownian probes for near-field investigations of the intracellular environment (Ph.D. thesis), École Polytechnique Fédérale de Lausanne, 2013.
[19] M. Grimm, S. Jeney, T. Franosch, Brownian motion in a maxwell fluid, Soft Matter 7 (5) (2011) 2076–2084.
[20] H. Clercx, P. Schram, Brownian particles in shear flow and harmonic potentials: A study of long-time tails, Phys. Rev. A 46 (4) (1992) 1942.
[21] B. Lukić, S. Jeney, Ž Sviben, A.J. Kulik, E.-L. Florin, L. Forró, Motion of a colloidal particle in an optical trap, Phys. Rev. E 76 (1) (2007) 011112.
[22] T. Franosch, M. Grimm, M. Belushkin, F.M. Mor, G. Foffi, L. Forró, S. Jeney, Resonances arising from hydrodynamic memory in Brownian motion, Nature 478 (7367) (2011) 85–88.
[23] G. Poppe, C. Wijers, Algorithm 680: evaluation of the complex error function, ACM Trans. Math. Software 16 (1) (1990) 47.
[24] T. Winiecki, Complex scaled complementary error function, 2007. http://www.mathworks.com/matlabcentral/fileexchange/12091.
[25] R. Zwanzig, M. Bixon, Hydrodynamic theory of the velocity correlation function, Phys. Rev. A 2 (5) (1970) 2005.
[26] M. Grimm, T. Franosch, S. Jeney, High-resolution detection of Brownian motion for quantitative optical tweezers experiments, Phys. Rev. E 86 (2012) 021912.
[27] S. Jeney, F. Mor, R. Koszali, L. Forró, V.T. Moy, Monitoring ligand–receptor interactions by photonic force microscopy, Nanotechnology 21 (25) (2010) 255102.

Further reading

[1] E.J. Hinch, Application of the Langevin equation to fluid suspensions, J. Fluid Mech. 72 (1975) 499–511. 12.
[2] P. Domínguez-García, F. Cardinaux, E. Bertseva, L. Forró, F. Scheffold, S. Jeney, Accounting for inertia effects to access the high-frequency microrheology of viscoelastic fluids, Phys. Rev. E 90 (2014) 060301.
[3] P. Domínguez-García, F.M. Mor, L. Forró, S. Jeney, Exploiting the color of Brownian motion for high-frequency microrheology of Newtonian fluids, Proc. SPIE 8810 (2013) 881015–881015-6.